JMEPEG (2021) 30:6588–6605
https://doi.org/10.1007/s11665-021-05927-6

1059-9495/$19.00

Studying the Microstructural Effect of Selective Laser Melting and Electropolishing on the Performance of Maraging Steel

D. Ahmadkhaniha, H. Möller, and C. Zanella

Submitted: 18 December 2020 / Revised: 27 April 2021 / Accepted: 7 May 2021 / Published online: 2 June 2021

Selective laser melting is one of the additive manufacturing technologies that have been known for building various and complicated shapes. Despite numerous advantages of additive manufacturing technologies, they strongly influence the microstructure and typically show a relatively high surface roughness. In this study, maraging steel was produced by selective laser melting (SLM), and its microstructure, hardness and corrosion behavior before and after heat treatment were studied and compared to traditionally manufactured ones (wrought, forged samples). In addition, the effect of electropolishing on the surface roughness was evaluated. The microstructural study was carried out by scanning electron microscopy equipped with electron backscattered diffraction in three different sections: parallel to the top surface (*xy*), transverse cross section (*xz*) and longitudinal cross section (*yz*). The same characterization was applied to heat-treated samples, austenitized and quenched as well as the aged ones. The results showed that selective laser melting produced a fine grain martensitic structure (in the as-printed condition) with a surface roughness (R_a) of about 10 µm. There was no sign of preferred texture or anisotropy in the microstructure of as-print SLM materials. The SLM microstructure was similar in all 3 sections (*xy*, *xz* and *yz*). Despite finer microstructure, nano-hardness and corrosion behavior of SLM and conventional wrought maraging steel in heat-treated conditions were similar. Aging resulted in the maximum nano-hardness and the minimum corrosion potential values. Precipitation has the main role in both hardness and corrosion behavior. Electropolishing was optimized and reduced the surface roughness (R_a) by 65%.

Keywords corrosion behavior, electropolishing, maraging steel, microstructure, SLM, surface roughness

1. Introduction

Additive manufacturing (AM), also known as three-dimensional printing (3D printing), is a family of technologies that fabricates objects directly from a 3D model by printing layers by layers (Ref 1, 2). Computer-aided design (CAD) data is used to derive the cross section for each layer. AM is classified into different types according to ASTM52900. For metal powder materials, powder bed fusion (PBF), which includes selective laser melting (SLM) or electron beam melting (EBM), is the most widely used 3D printing technology (Ref 1, 3, 4). In the selective laser melting process, the powders are locally melted by the laser radiation, forming molten pools, which then solidify and metallurgically bond to the previously molten layer (Ref 3, 5, 6).

Maraging steels are mainly applied in the aerospace and tool-manufacturing industries, which often need components with complex geometry and excellent mechanical properties in relatively small quantities (Ref 7, 8). Maraging steel has also been used for the manufacturing of molds for plastic products. For this application, SLM is a useful technique which, in contrast to the conventional cast, can produce molds with complex internal cooling channels even located close to the surface.

Since the functionality and properties of materials are determined by their microstructure (Ref 9, 10), it is vital to consider the microstructure of the material produced by AM. Due to the rapid cooling rates and layered solidification in AM processing, the material microstructure is different from its cast and wrought counterparts (Ref 11, 12). Anisotropic and non-equilibrium microstructures, including metastable phases, porosity, unmelted powder and gas entrapment, have been observed for AM materials (Ref 1, 4, 13-15). Due to the planar movement of the heat source and uniaxial movement of the build plate, achieving a homogenized microstructure and isotropic mechanical properties in as-printed maraging steel is challenging (Ref 14). Different researchers such as Kempen et al. (Ref 16), Casalino et al. (Ref 17), Tan et al. (Ref 7), Bai et al. (Ref 8) and Suryawansi et al. (Ref 18) have focused on the influence of SLM process parameters and heat treatment on mechanical properties of maraging steel, while there have been

This invited article is part of a special topical focus in the *Journal of Materials Engineering and Performance* on Additive Manufacturing. The issue was organized by Dr. William Frazier, Pilgrim Consulting, LLC; Mr. Rick Russell, NASA; Dr. Yan Lu, NIST; Dr. Brandon D. Ribic, America Makes; and Caroline Vail, NSWC Carderock.

D. Ahmadkhaniha, School of Engineering, Jönköping University, Gjuterigatan 5, P.O. Box 1026, Jönköping, Sweden; **H. Möller**, School of Engineering, Jönköping University, Gjuterigatan 5, P.O. Box 1026, Jönköping, Sweden; and Department of Materials Science and Metallurgical Engineering, University of Pretoria, Pretoria, South Africa; and **C. Zanella**, School of Engineering, Jönköping University, Gjuterigatan 5, P.O. Box 1026, Jönköping, Sweden; and Department of Industrial Engineering, University of Trento, via Sommarive 11, Trento, Italy. Contact e-mail: donya.ahmadkhaniha@ju.se.

less comprehensive studies on the microscopic features of maraging steel produced by SLM. In addition, the effect of the microstructure of maraging steel manufactured by SLM on corrosion behavior remains unclear.

Apart from the different microstructure than cast samples, AM samples are known to have relatively rough surfaces. Different parameters such as powder size, layer thickness, scanning parameters and laser energy can affect the surface roughness of the samples. Surface quality in AM parts is greatly affected by the ''stair-step'' effect, which is the stepped approximation by layers building inclined surfaces. The layer thickness can be reduced to improve the surface finish. Moreover, if layer thickness is comparable to particles diameter, the particles stuck along step edges can fill the gaps between consecutive layers, hence affecting the actual surface roughness (Ref 19). High scan speed can result in some unmelted powders, which affect the surface roughness as well. During the SLM process, the laser molten track possesses a shrinking tendency to decrease the surface energy. Thus, the balling phenomenon happens during the SLM process, which is detrimental to the quality (Ref 20). Selective laser melting is one of the additive manufacturing processes that can produce samples with a lower surface roughness than the rest (Ref 21-24). However, in general, additive manufacturing samples have higher surface roughness than conventionally produced samples (Ref 25).

Rough surfaces can cause premature fatigue failure due to increased stress concentrations near the material surface (Ref 26-28). Moreover, rough surfaces can affect other functional properties such as specific energy absorption, corrosion behavior, fluid dynamics and optical properties (Ref 29, 30). Therefore, surface quality has to be improved by suitable post-processing. Different post-processing methods such as milling on maraging steel and high strength low alloy steel (HSLA) and blasting on CoCr alloy, laser polishing and chemical polishing on 316 stainless steel have been applied for additive manufacturing parts (Ref 23, 31-33). However, they might not be proper for complex geometries with undercuts or inner structures. In most of the post-processing methods, the external surface roughness can be modified while they cannot access most internal surfaces, for instance, lattices. In addition, some of the mechanical post-processing might break delicate structures.

In this study, electropolishing was applied to reduce the surface roughness of SLM maraging steel. Electropolishing (EP) is an electrochemical process that is carried out in an electrolytic cell, including two electrodes (anode and cathode), a power supply and an electrolyte (Ref 34). The sample is connected as the anode, and a high corrosion-resistant material (such as stainless steel or platinum) is used as a cathode. The anode and cathode are immersed in an electrolyte, and an electric current is externally applied. As current passes through the sample (anode), the protrusion of the surface, which has a higher current density, will be corroded faster than the surface valleys (Ref 35). Electropolishing has been applied to AM samples to reduce surface roughness, especially for stainless steel and Ti alloy components. Su et al. (Ref 22) obtained a smoother, brighter and more corrosion-resistant steel by electropolishing. Pyka et al. (Ref 36) reduced the surface roughness of additive manufactured Ti6Al4V by electropolishing technique. However, there has not been any literature on electropolishing of SLM maraging steel. Therefore, this study was designed to investigate the effect of SLM on the microstructure and electropolishing as a post-processing method on the surface roughness of maraging steel. Finally, the corrosion behavior of maraging steel in the as-printed and heat-treated condition was compared.

2. Materials and Experimental Methods

2.1 Materials and Characterization

The as-printed (AP) maraging steel with a dimension of 10 * 5 * 0.3 cm^3 was fabricated by SLM (SLM Solutions 280 machine) at the University of Pretoria. Heat treatments were applied on some of the samples categorized as AQ (austenitized at 900 °C for 30 min and quenched in water) and AG (AQ and then heating at 460 °C for 3 h). The samples were sectioned to investigate the microstructure on different planes, *xy*, *xz* and *yz* as shown in Fig. 1.

Conventional wrought maraging steel (cast, forged and AQ) with a diameter of 4 cm and length of 1 m was provided by Matmatch GmbH company as a benchmark representing a traditional production route. The conventional samples were cast and forged, then austenitized and quenched at 900 °C for 30 min. The AQ condition for SLM sample was chosen according to the one that was commercially used for the conventional sample, so they were comparable (Matmatch GmbH). AG condition (heating 460 °C for 3 h) was chosen according to the literature review (Ref 7, 37). The composition of the as-print and conventional maraging steel was determined by energy-dispersive spectroscopy (EDS), and the results are listed in Table 1.

Conventional samples were cut from a bar, and since the sample has cylindrical symmetry, in this study, just *xy* (bar section) and *yz* (longitudinal section) planes were characterized.

The samples were mechanically polished, followed by etching with two solutions, Nital (3 vol.%) and Fry's reagent ($CuCl_2$: 5 g, HCl: 40 ml, H_2O: 30 ml, C_2H_5OH: 25 ml) at room temperature. Nital was used to preferentially etch the alloy-rich segregations regions and remark the solidification substructure. On the other hand, Fry's reagent reveals the martensitic morphology (Ref 38). The microstructures were observed using OM (optical microscope, Olympus, GX71F) and SEM (scanning electron microscope, SEM, JEOL 7001F), operating at 15 kV with secondary electron and equipped with EDS (energy-dispersive spectroscopy). The grain orientation was analyzed by electron backscattered diffraction (EBSD) with a 0.05-µm step size. The density of SLM samples was measured for three different samples, using the Archimedes principle, and the porosity of the samples was measured according to Eq 1.

$$\text{Porosity} = 100\,(1 - \rho/\rho_m) \quad \text{(Eq 1)}$$

where ρ_m is 8.1 g/cm^3, and ρ is the density of the immersed sample in distilled water.

The nano-hardness of the samples was measured by Berkovich indenter (NanoTest™ Vantage) at 100 mN for 10 s dwell time. Fifteen measurements were run (on two samples with the same conditions) on the center line of *xy*, *xz* and *yz* planes (the same planes for microstructural analysis), and the average and standard deviation values were reported. The surface roughness of the samples on the *xy* plane before and after electropolishing was measured by a contact surface profilometer (Surtronic 3 plus). Two measurements on a 12.5-

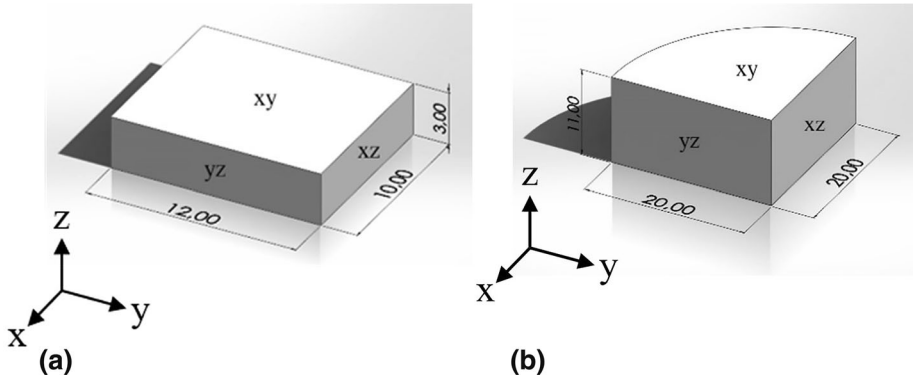

Fig. 1. Schematic of different sections in (a) SLM, building direction was along z axes, (b) conventional maraging steel; all the units are in mm

Table 1 Chemical composition (wt.%) of conventional and SLMed maraging steel

Processing method	Fe	Ni	Mo	Co	Ti	V	Si	S	Mn
SLM	69.6 ± 0.6	15.8 ± 0.5	3.2 ± 0.4	7.6 ± 0.5	0.9 ± 0.2	0.3 ± 0.0	1.70 ± 0.30	0.1000 ± 0.0000	0.4 ± 0.1
Conventional (UNS K93120)	72.2 ± 0.6	17.1 ± 0.1	2.7 ± 0.2	6.4 ± 0.2	1.2 ± 0.0	…	0.04 ± 0.00	0.0018 ± 0.0000	0.3 ± 0.0

mm line parallel to x and y axes were done on each sample, and the average value was reported as R_a. Surface roughness was also measured on 0.49 cm^2 area on xy plane by confocal microscope (μSurf Explorer, Nanofocus). Two measurements on two samples with the same conditions were done, and the average values of surface roughness were reported. The edges of the samples were not considered for the surface roughness measurements.

Confocal microscope measures surface profiles and roughness by the white light interferometry. The software calculates surface properties according to the ISO25718 standard. For the quantitative analysis, the following parameters were determined; arithmetic mean height over the surface (S_a), Eq 2, root mean square of height over the surface (S_q), Eq 3, the maximum peak height (S_p), Eq 4, the maximum valley depth (S_v), Eq 5 and the maximum height difference between peak and valley (S_z), Eq 6.

$$S_a = \frac{1}{A}\int_0^A \int Z(x,y)\mathrm{d}x\mathrm{d}y \quad \text{(Eq 2)}$$

$$S_q = \sqrt{\frac{1}{A}\int_0^A \int Z^2(x,y)\mathrm{d}x\mathrm{d}y} \quad \text{(Eq 3)}$$

$$S_p = \underset{A}{\overset{\mathrm{Max}}{}} Z(x,y) \quad \text{(Eq 4)}$$

$$S_v = \underset{A}{\overset{\mathrm{Min}}{}} Z(x,y) \quad \text{(Eq 5)}$$

$$S_z = S_p + S_v \quad \text{(Eq 6)}$$

The corrosion behavior of the samples was measured by the polarization technique (potentiostat, Ivium). For this purpose, 1 cm^2 of xy plane of the samples was exposed to 0.5 M Na_2SO_4 at room temperature. Ag/AgCl (3M KCl, 0.21 versus SHE/V) and platinum electrodes were used as the reference and counter electrodes, respectively. The anodic potentiodynamic polarization was performed after 20 min delay in the potential range − 50 mV to 1 V with respect to the open circuit potential (OCP) with a scan rate of 0.2 mV s^{-1}.

Besides, samples were immersed in 0.1 M NaCl for 1 day to examine their pitting corrosion. After the immersion test, the samples were rinsed with citric acid to remove corrosion products, and the sample surfaces were examined by SEM. Polarization and immersion tests were repeated at least twice for each condition to have repeatable and valid results.

2.2 Electropolishing

Electropolishing was carried out in 60 vol.% phosphoric acid, 30 vol.% sulfuric acid, 9.7 vol.% DI water with glycerol (0.3 vol.%) at 60 °C. Maraging steel was the anode, and a conductive oxide net was chosen as the cathode. A magnetic stirrer with 1 cm length and 4 mm diameter was used to stir the electrolyte at 150 rpm, and the distance between the anode and cathode was 4 cm. Electropolishing was carried out for different potentials (1.5-6 V) and time (10, 20 and 30 min) on as-printed samples. For each condition, 3 experiments were carried out, and the average surface roughness was reported.

3. Results and Discussions

3.1 Optical and SEM Microscopy

Optical images of different sections in SLM and conventional samples are shown in Fig. 2 and 3. AP samples (Fig. 2a, d, g) showed a very fine microstructure, and after AQ, the martensitic microstructure was revealed (Fig. 2b, e, h). SLM process includes a rapid cooling rate during and after solidification (up to 10^6 °K s^{-1}) which can result in the martensite microstructure of AP maraging steel. Thinner and denser

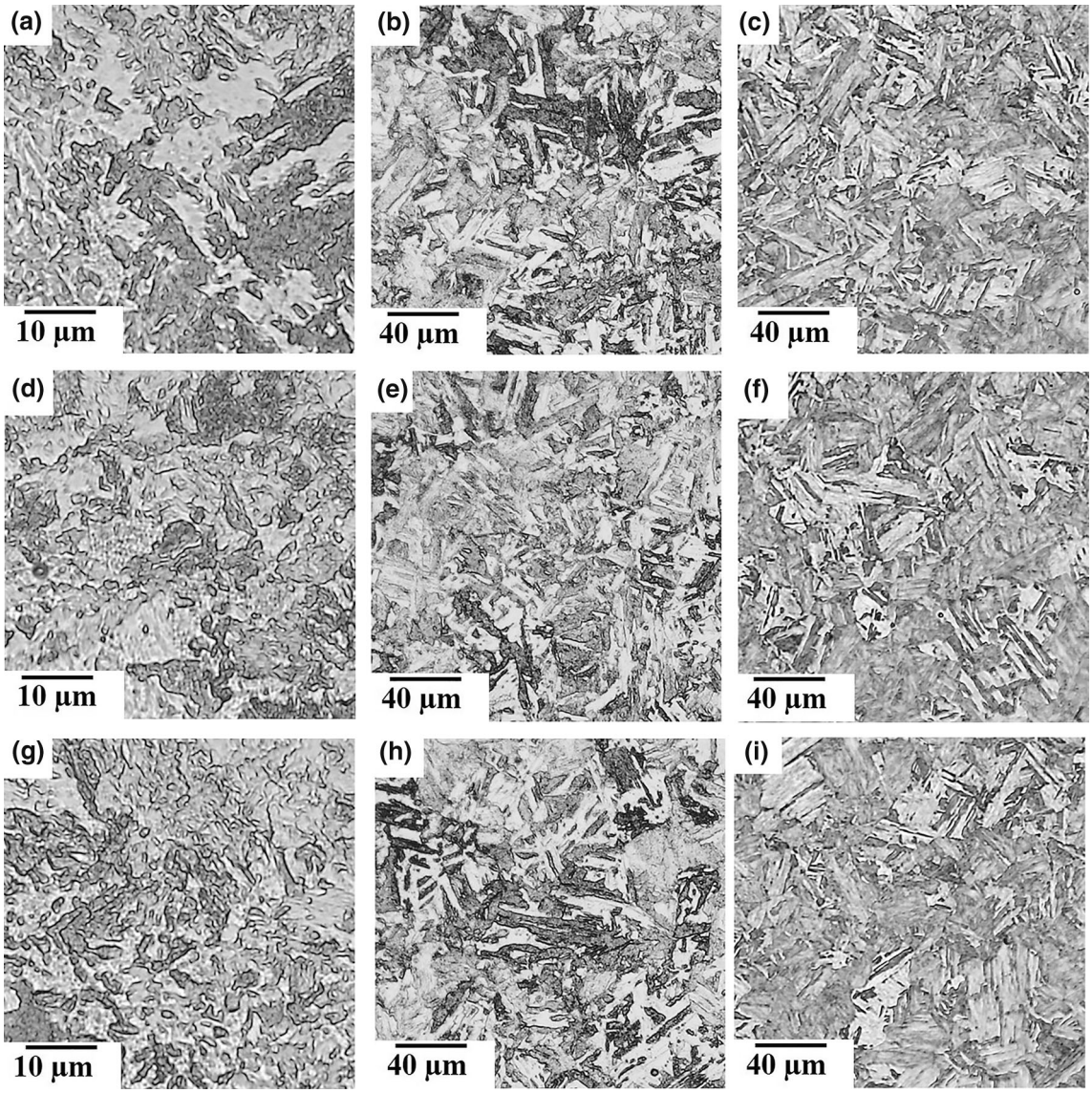

Fig. 2. Optical micrograph images of SLM samples, (a, d, g) AP, (b, e, h) AQ, (c, f, i) AG, (a-c) *xy*, (d-f) *yz*, (g-i) *xz*. Samples were etched with Fry's solution.

martensite laths were formed by AG than by AQ (Fig. 2c, f, i). Each lath in the martensitic structure is a result of a homogeneous shear, the basic laths are generally aligned parallel to each other in groups that have been known as a packet which includes a high density of tangled dislocations, and several packets can be found within a prior austenite grain (Ref 39).

Conventional samples (Fig. 3a, c) have similar martensitic microstructure with coarser and less density of martensite laths to the one in AQ, SLM samples (Fig. 2b, e, h). In addition, some coarse grains besides thin martensites can be observed in AQ conventional samples. The difference in the martensitic microstructure of SLM and conventional samples is due to the different thermal gradients and cooling rate of the manufacturing processes. Solution treatment before aging is necessary for the maraging steel manufactured by casting and forging methods to prepare the martensite matrix for precipitation strengthening. While for maraging steel produced by SLM, due to the rapid cooling, the martensite matrix has been achieved during SLM manufacturing process (Ref 8, 40). This initial microstructure also affects the final martensitic microstructure after AQ. Aging produced thinner martensite laths than AQ in the conventional sample. For a better comparison between the microstructure of SLM and conventional samples after aging, EBSD analysis was used, which have been discussed in Sect. 3.2.

According to optical images (Fig. 2, 3), the microstructure of different sections (*xy*, *yz* and *xz*) has comparable martensitic microstructure in both SLM and conventional samples even after applying heat treatments.

Figure 4 shows SEM graphs of different sections of the AP specimen. The boundaries of melt pools are well noticeable (Fig. 4a) after etching with Nital. During SLM, the maximum thermal gradient is at the leading edge of the laser beam and the thermal gradient influences the scan track growth (Ref 41). Hence, faster cooling happens at the leading edge of the laser beam, and it leads to a semi-elliptical shape (Ref 7, 41). Melt pools have 98 ± 15 and 58 ± 5 µm depth and width, respec-

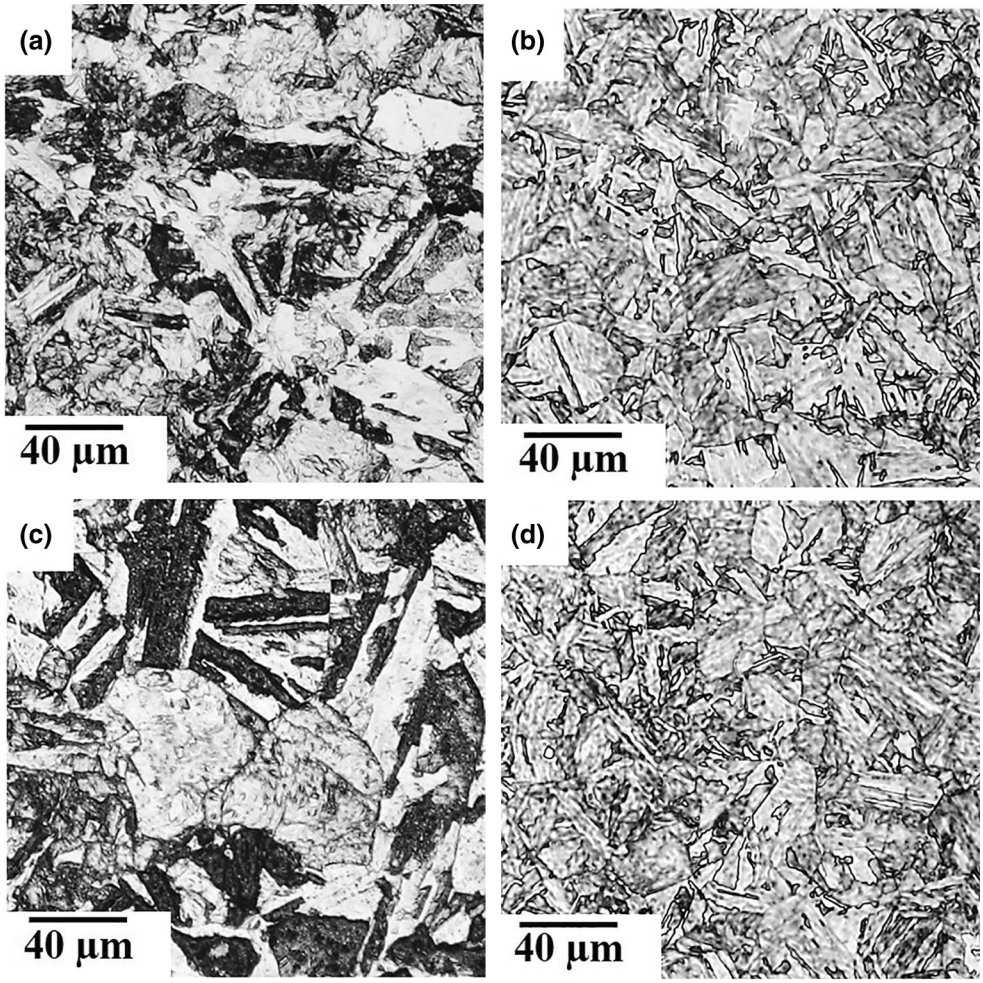

Fig. 3. Optical micrograph images of the conventional wrought sample (a, c) *xy* (b, d) *yz* (a, c) AQ, (b, d) AG. Samples were etched with Fry's solution

tively. The size of melt pools depends on several parameters, such as the input power, exposure time, spot distance and the beam size at the focal point (Ref 42).

The fine cellular substructure is depicted along with elongated cells (shown by arrows) in Fig. 4(b). Since cooling rates in SLM can be in the high order of 10^6-10^7 K s^{-1} (Ref 7), materials experience fast solidification far from equilibrium conditions due to the severe temperature gradients. This complicated thermal process leads to a complex microstructure (Fig. 4c), including columnar dendritic structures at the bottom of the molten pool, cellular microstructures in the middle of the molten pool and coarse equiaxial crystal at the border between the molten pools. The columnar dendrites grow according to the thermal gradient, and the solute enrichment of the liquid in front of the solid–liquid interface determines the constitutional undercooling (Ref 17). The microstructure depends on the ratio between the temperature gradient and the solidification rate; therefore, a cellular dendritic structure is formed along with the heat flow. The coarse equiaxial crystals are formed at the borders between the molten pools since this region is affected by the heat flux of the subsequent laser irradiation (Ref 7).

After AQ, the traces of the scan tracks and solidification disappeared, and the cellular structure was replaced by massive martensite microstructure, as seen in Fig. 4(d). Tan et al. (Ref 43) also observed the same microstructure changes by heat treatment.

3.2 EBSD

Figure 5 represents an inverse pole figure (IPF) map of the samples. The representative colors in the IPF map correspond to the crystallographic orientations normal to the observed plane, as indicated by the stereographic triangle in the picture. In the IPF map, melt pools cannot be recognized since grains cross the melt pool boundaries due to epitaxial growth (shown by arrows in Fig. 5b). During the melting of adjacent beads, partial remelting happens, which allows the formation of new grains with the same crystallographic orientation as the nearby grains (Ref 44). Epitaxial growth of new grains from remelted zones, following maximum temperature gradient directions, was also observed in Fig. 4(b) (shown by arrows).

Figure 5(c) shows the phases map detected by EBSD, which indicates a martensitic microstructure. There is a low fraction of retained austenite in the structure (green areas) distributed mainly in melt pool boundaries. The presence of austenite can be due to the re-transformation of martensite to austenite during subsequent melting of an overlying powder layer which causes a constant heat flow from the molten regions to the building platform (Ref 45). Jägle et al. (Ref 46) reported that austenite

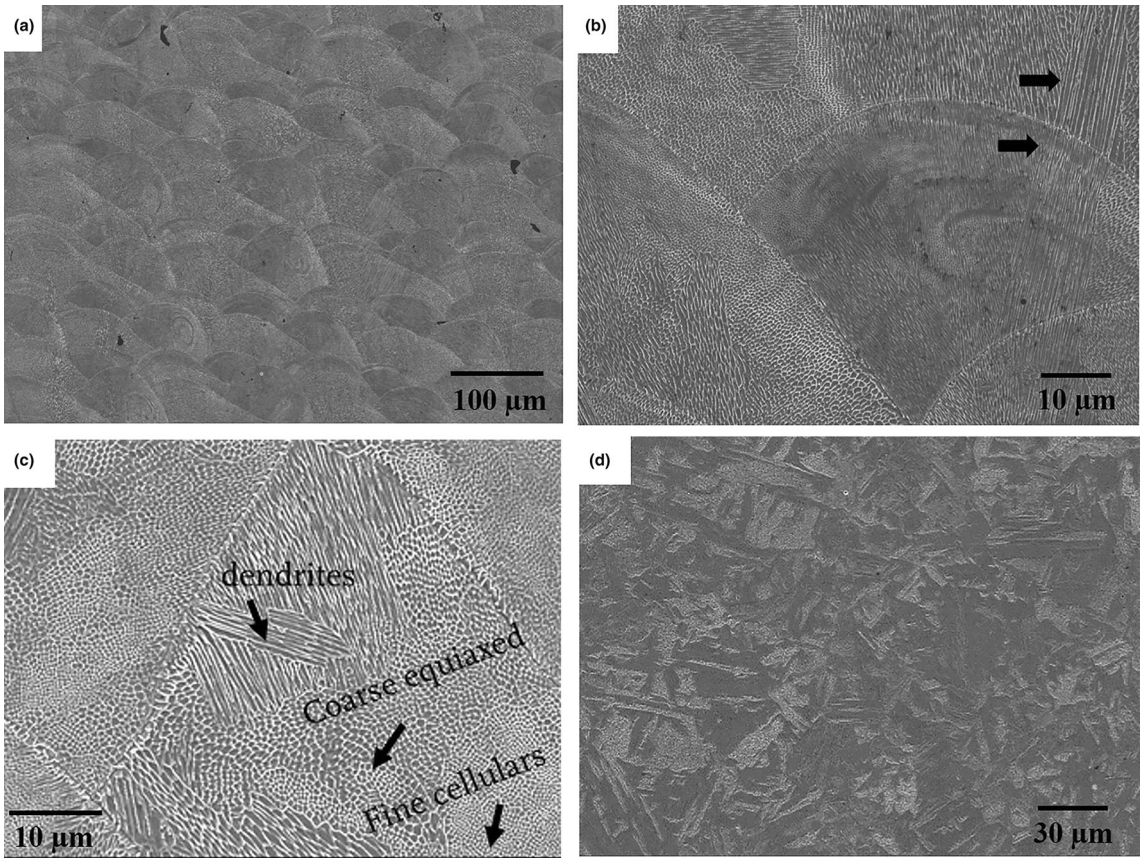

Fig. 4. SEM images of SLM sample, *yz* plane (a) melt pool boundaries, AP, (b, c) high magnification of the melt pools, AP (d) after AQ

appears in the interdendritic regions since interdendritic areas are enriched with Ti, Mo and Ni due to microsegregation. The amount of martensite-to-austenite transformation depends on the local composition. Even though Ti and Mo are ferrite stabilizing elements, it was shown that austenite is stable to lower temperatures than ferrite in interdendritic zones (Ref 46).

The IPF orientation maps, obtained through EBSD, of different planes (*xy*, *yz* and *xz*) of the AP sample are seen in Fig. 6. The grain boundaries of AP samples exhibit a high degree of tortuosity, which has been seen in materials containing a consistent distribution of grain boundary precipitates and/or eutectic constituents. The precipitations and eutectic constituents pin the grain boundary motions and prevent grain growth (Ref 47, 48).

For a better demonstration of grains, grain boundaries maps are shown in Fig. 6(d)–(f) Since martensite laths follow a specific orientation relationship with prior austenite grains, they maintain a small misorientation within a block. Hence, the rotation angle of the substructure boundaries of lath martensite is below 5° (red lines in Fig. 6d–f). Blocks subdivided from packets maintain relatively larger misorientation with respect to laths and contribute to the formation of LAGBs (rotation angle ranges from 5° to 15°, green lines), while packets formed along different habit planes in an austenite grain typically exhibit remarkable crystallography misorientations, the HAGBs (rotation angle ranges from 15° to 180°, blue lines). Therefore, HAGBs were constituted of both packets boundaries and prior austenite boundaries (Ref 45).

According to Fig. 6, the microstructure of AP in all *xy*, *yz* and *xz* sections mainly consists of refined grains, but some coarse grains also exist due to the heat from the subsequent layer deposition (Ref 45). In addition, the length of LAGB and HAGB is comparable for *xy*, *yz* and *xz* sections which means the martensite's laths, blocks and packets have similar size as well.

There is no preferred texture in SLM samples according to Fig. 6 since the texture intensity (for all sections), which demonstrates the intensities of the number of *hkl* planes in the reflecting condition, is less than 4. Texture evolution related to the thermal process parameters such as heat flow direction, cooling rate and temperature gradient and these parameters depend greatly on SLM process parameters (Ref 49). The absence of preferred texture can be due to the rotation of laser scanning between the layers that changed the heat flux direction. The same results were also obtained by Suryawanshi et al. (Ref 18), who observed the absence of cubic texture along build direction in 3D printed maraging steel by 90° rotation of laser scanning between successive layers. Casati et al. (Ref 42) also reported that rotation of scanning direction by 67° after each layer results in an almost isotropic polycrystalline material.

The IPFs of *xy* plane after heat treatment (AQ and AG) are shown in Fig. 7, which display the lath martensite structures with sharp boundaries in heat-treated samples. In addition, prior austenite grains with martensite packets inside can be seen. Aging refined the microstructure with respect to AQ condition. Conde et al. (Ref 12) observed complete austenitization by tempering at 690 °C; also, grain refinement was promoted when compared to the as-built condition.

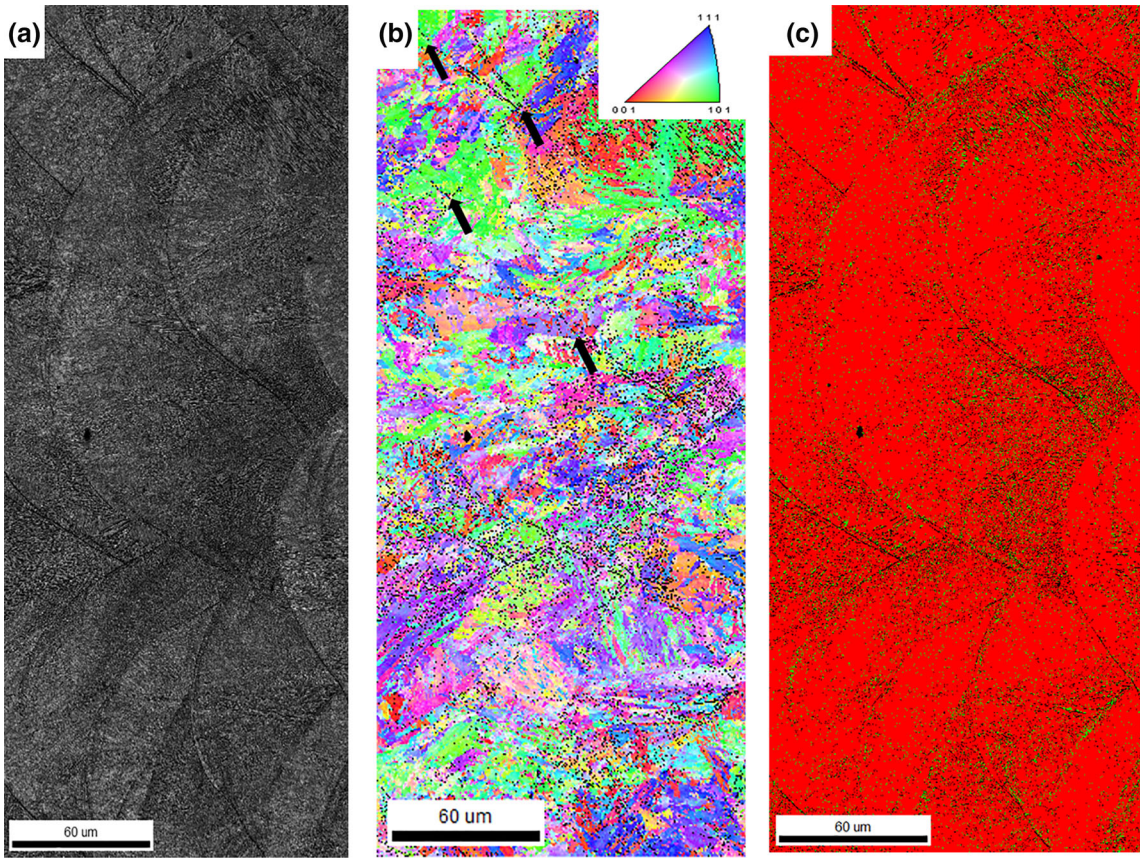

Fig. 5. (a) SEM, (b) IPF, (c) phase map (martensite with red color and austenite with green color) images of etched AP sample, *yz* plane (Color figure online)

To compare the effect of heat treatment on the microstructure, the average grain size of the samples was calculated. The mean grain size of the lath martensite structure was estimated by the equivalent grain size, which is calculated by the total length of the HAGB per unit area (Ref 50). According to Ueji et al. (Ref 51), there is a relationship (Eq 7) between S_v (the length of HAGB per unit area) and the mean intercept length (L) for any three-dimensional shape of masses.

$$S_v = \frac{2}{L} \qquad \text{(Eq 7)}$$

where L can be considered as the mean grain size of the lath martensite structure. The grain size values for different samples are summarized in Table 2.

According to the data in Table 2, the minimum grain size was in AP condition, and by AQ, the grain size was increased while AG refined the microstructure of AQ one. The increase in grain size after AQ can be attributed to relief of internal stress induced during SLM processing after heat treatment as well as grain growth during austenitizing. While by aging due to the precipitation, the movement of the grain boundaries is limited, and the grain growth is reduced, which decreased the grain size. In the study by Mutua et al. (Ref 52), almost the same average grain size for the as-built and aged specimens was obtained while the martensite grains in the matrix were grown in solution treatment/aging.

IPFs of conventional samples are shown in Fig. 8, which demonstrate coarse grain structure with respect to SLM ones due to the lower cooling rate in the casting process. The grains in *xy* and *yz* sections have a similar orientation. Since there was no difference in the microstructure of different planes in AQ conditions, only *xy* plane is reported after aging (Fig. 9). According to Fig. 9, aging did not affect the microstructure noticeably (similar mean grain size value to AQ one, Table 2), while the texture intensity decreased to 1.9. It should be noted that many previous investigations (Ref 49, 53, 54) reported that post-annealing weaken or even randomize the texture.

Table 2 summarizes the mean grain size and the austenite fraction of the samples in different conditions. A higher amount of the austenite in SLM sample with respect to the conventional one can be due to the formation of retained austenite. According to Callister et al. (Ref 55), the occurrence of retained austenite is more possible at grain boundaries where the atomic arrangement is irregular, and further growth of martensite is not possible. Gao et al. (Ref 56) also found more austenite in SLM maraging stainless steel than in the conventional one. They ascribed this observation to the finer microstructure and larger residual stress, which provides a larger driving force for austenitic transformation and, therefore, reduces the austenite finish temperature. Sarkar et al. (Ref 57) also agreed that finer microstructure promotes the retained austenite formation. Moreover, they found more austenite in the solution treated samples than in the SLM ones. A higher amount of austenite in the solution treated sample can be attributed to the formation of the reverted austenite as a result of the non-diffusive martensite-to-austenite transformation during

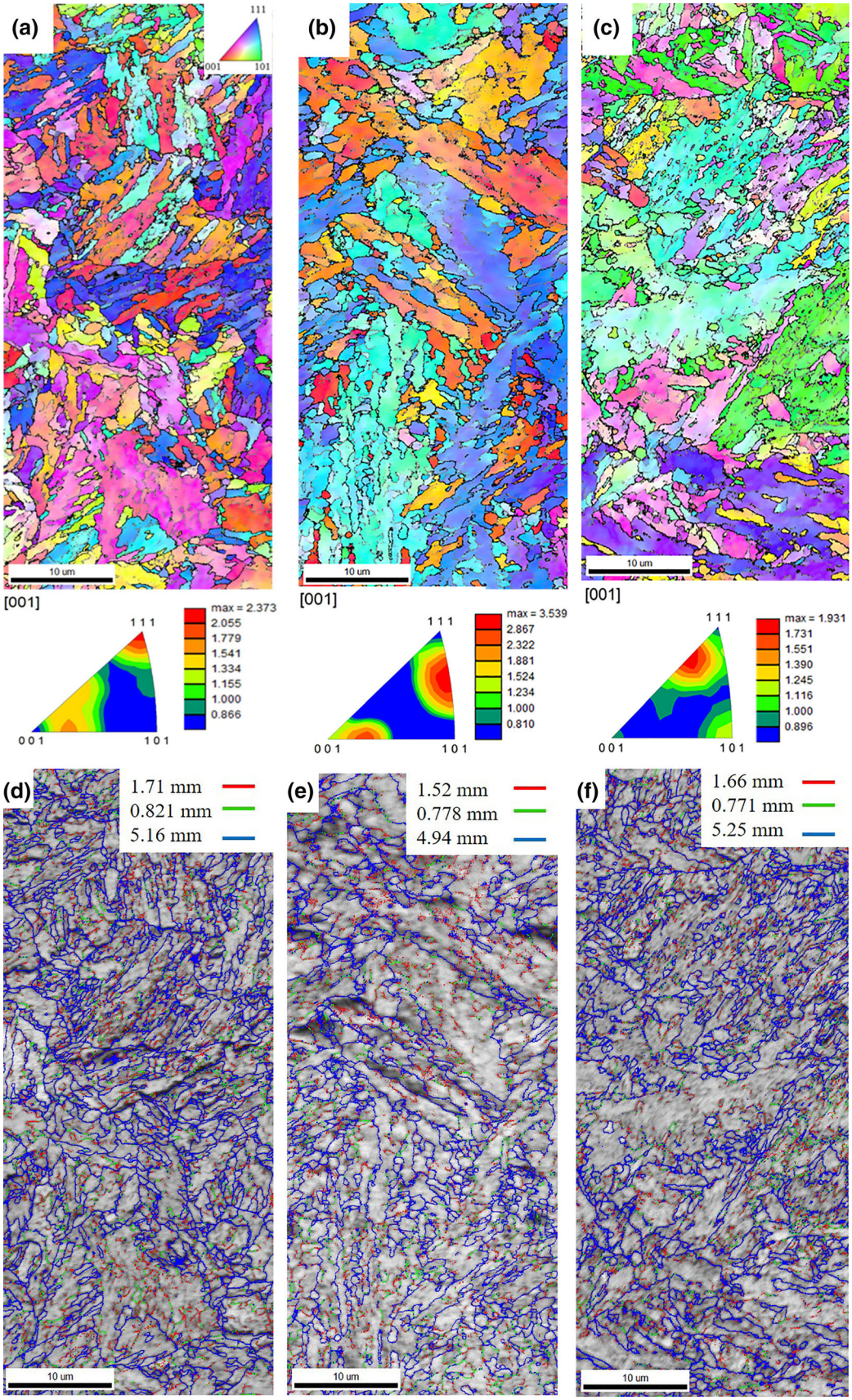

Fig. 6. IPFs and grain boundary images of AP samples, (a, d) *xy*, (b, e) *yz*, (c, f) *xz* (Color figure online)

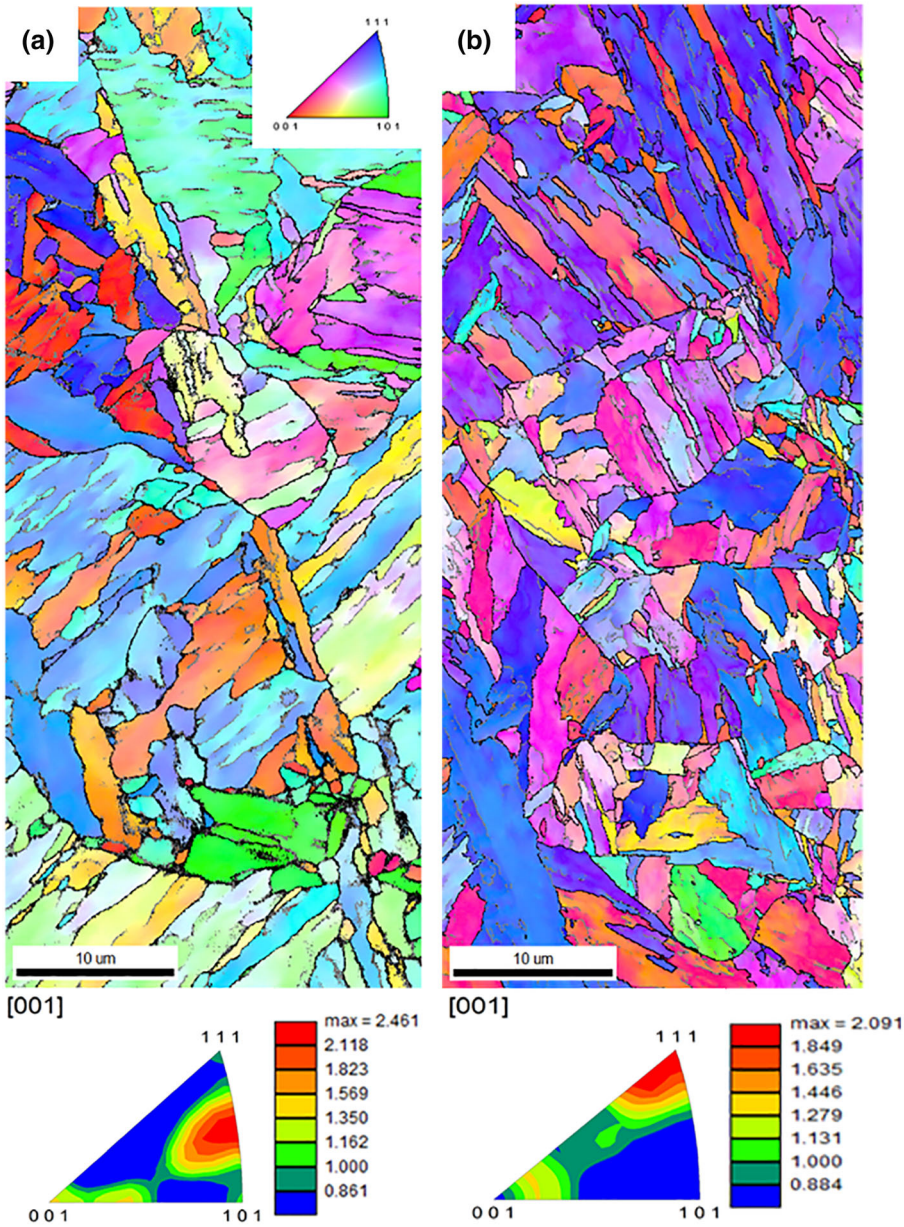

Fig. 7. IPFs of (a) AQ, (b) AG SLM sample, *xy* plane

Table 2 Mean grain size of the lath martensite and austenite fraction in SLM and conventional materials at different conditions

	AP, SLM	AQ, SLM	AG, SLM	AQ, C	AG, C
Mean grain size of the lath martensite, μm^2	0.64 ± 0.1	1.58 ± 0.1	1.05 ± 0.3	2.85 ± 0.5	2.26 ± 0.7
Austenite fraction	0.32	0.49	0.56	0.07	0.32

subsequent aging. Therefore, higher austenite was found in aged sample since it includes both reverted austenite and retained austenite which cannot be distinguished by XRD and EBSD analysis because of the same face-centered cubic (FCC) crystalline structure. Reduction of retained austenite by solution annealing and formation of reverted austenite by aging were also observed by other researchers (Ref 57-59). However, the difference in the fraction of austenite in different conditions is not significant.

3.3 Nano-Hardness

The nano-hardness values of SLM samples were measured at 100 mN load, and the results are listed in Table 3. Since there was no significant difference in the hardness values of different sections in SLM and conventional samples, only the results related to *xy* are shown. Higher nano-hardness values in AP samples than the AQ can be related to the smaller mean grain size and stress-relieving effects of AQ. In AP samples, during

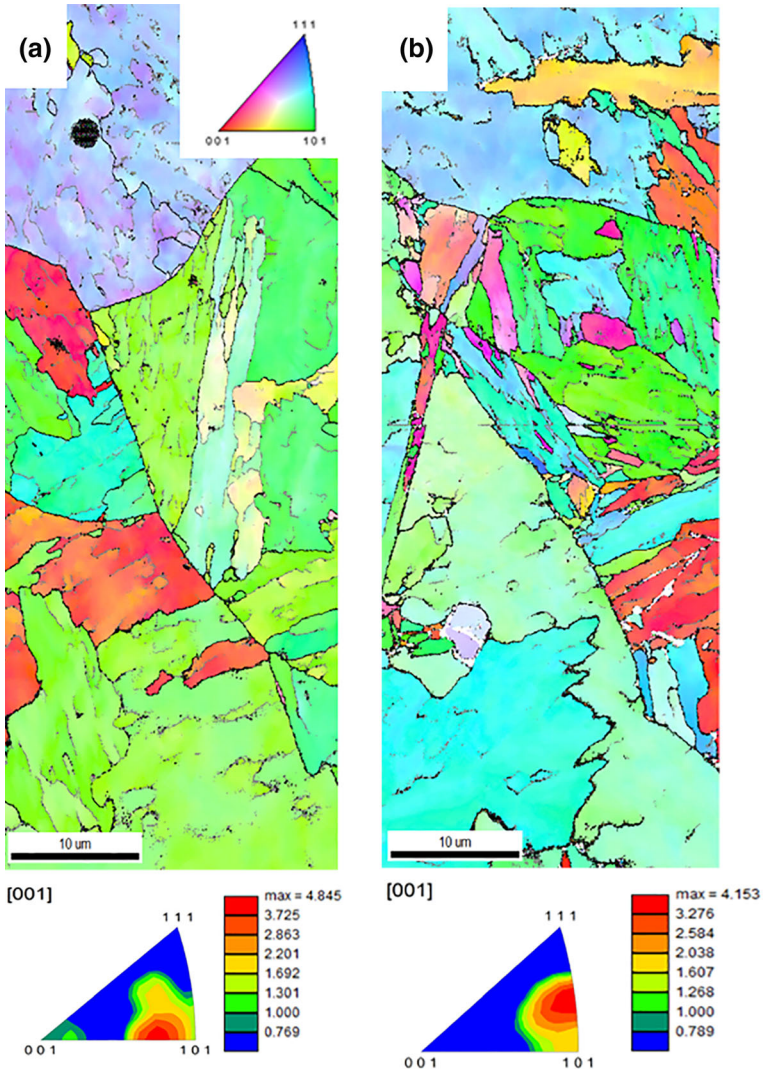

Fig. 8. IPFs of AQ conventional samples (a) *xy*, (b) *yz*

the rapid solidification process, internal stress and high concentration of dislocation at the subgrain boundaries along with relatively high LAGB were obtained, which was be reduced by AQ. Similar nano-hardness values for AQ samples (SLM and conventional) were obtained, even though their mean grain size is different.

Aging for 30 min resulted in the maximum nano-hardness values (6 GPa) in both SLM and conventional samples. The increase in the nano-hardness values by aging has also been observed by others (Ref 14, 60) which can be attributed to the formation of fine precipitates of intermetallic compounds such as Ni_3Ti in the martensite matrix (Ref 52).

Conventional and SLM samples have similar nano-hardness values regardless of the larger mean grain size in the conventional sample. According to the nano-hardness results, precipitation hardening is the main strengthening mechanisms in maraging steel regardless of the manufacturing process.

The elastic modulus of the sample, E_s, was calculated from the reduced Young's modulus (E_r) according to Eq 8 (Ref 61, 62).

$$\frac{1}{E_r} = \frac{1-\upsilon_s^2}{E_s} + \frac{1-\upsilon_i^2}{E_i} \quad \text{(Eq 8)}$$

E_r considers that elastic displacements occur in both the sample and the indenter, $E_{i,s}$ and $\nu_{i,s}$ are the elastic modulus and Poisson's ratio for the indenter and the sample, respectively. In this study, E_i is 1140 GPa, and ν_i and ν_s are 0.07 and 0.3, respectively (Ref 63). Table 3 summarizes the elastic modulus of the samples. It can be seen that even by changing the nano-hardness values via heat treatment, the elastic modulus did not change, not only in SLM samples but also in conventional ones. Bao et al. (Ref 64) found a relation between E_r and hardness (H), according to Eq 9.

$$E_r = 0.6647\sqrt{HR_S} \quad \text{(Eq 9)}$$

where R_s is recovery resistance and is defined by Eq 10.

$$R_s = \frac{P_m}{H_s^2} \quad \text{(Eq 10)}$$

P_m is the maximum load in nanoindentation, and H_s is the depth of elastic recovery. According to these equations (Eq 8, 9) and the values in Table 3, the recovery resistance of maraging steel was decreased by aging in both SLM and conventional

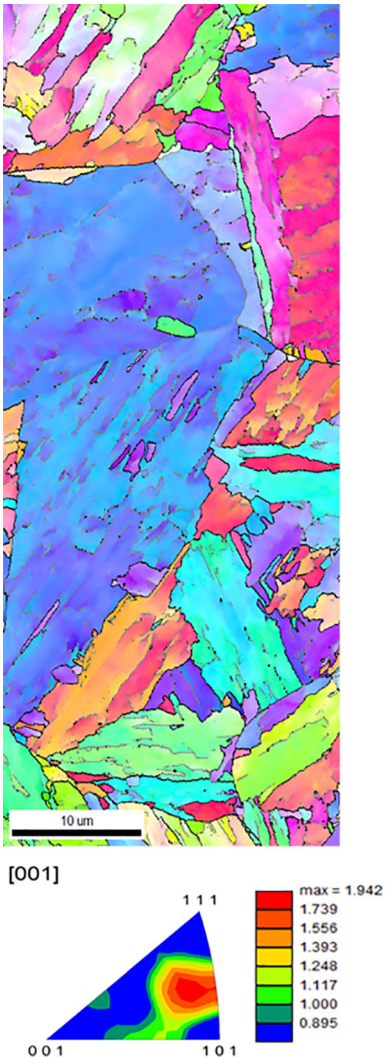

Fig. 9. IPF of AG conventional sample, *xy*

samples. As a result, higher hardness in aged samples did not result in higher elastic modulus.

3.4 Corrosion Behavior

The corrosion behavior of the mechanically polished (MP) samples on the *xy* plane was tested in 0.5 M Na_2SO_4 by polarization method, and the results are plotted in Fig. 10. According to Fig. 10(a), SLM maraging steel behaved like an active material and was corroded at a slow rate (i_{corr}: 4.7×10^{-6} A cm^{-2}). Heat treatment reduced the corrosion potential (E_{corr}) while corrosion current density (i_{corr}) was not affected, and AG sample has the minimum E_{corr} (see Table 4). It was reported that the austenitic phase formed during the aging thermal treatment was detrimental to the corrosion behavior of the 18Ni 300-grade maraging steel (Ref 65). Maraging steel is prone to corrosion mainly due to the martensitic matrix with intermetallic precipitates, such as Ni_3(Ti, Al, Mo). A galvanic coupling forms between the precipitates and the matrix, in which the α-Fe with lower potential plays as the anode and the precipitates act as the cathode. The micro-galvanic corrosion increased the dissolution rate of the matrix in AG samples. However, the average corrosion rate of AG SLM is similar to AP one (Fig. 10a), and this can be due to the formation of fine precipitates in these samples. SLM sample has a similar behavior as the conventional one (Fig. 10b).

It was reported that 3D printing could enhance the corrosion behavior of CoCr and CoCrW dental alloys; the opposite was noted in the Ti-6Al-4V alloy, which was attributed to its microstructure (Ref 1, 4, 52, 66). The better corrosion behavior of 3D printed Al-12Si alloy in 3.5 wt.% NaCl solution was also observed due to ultrafine eutectic Si particles in the microstructure, which stabilize the oxide layer that forms during the corrosion process (Ref 6). The improved corrosion behavior of 3D printed stainless steel in NaCl with different concentrations (0.1 and 0.6 M) has attained due to the reduction of inclusion concentration (Ref 6). On the other hand, the breakdown potential of 3D printed 316 L stainless steel in 3.5 wt.% NaCl solution was reduced, which was attributed to the pre-existing pores that get attacked preferentially during corrosion (Ref 67). Preferentially corrosion attack around porosities was also confirmed by other researchers (Ref 6, 68-70). In this study, the porosity of the SLM sample after AQ was $0.3\% \pm 0.1$, while in conventional samples after AQ was $0.1\% \pm 0.1$. Since the amount of porosity was negligible, they did not affect the corrosion behavior of SLM maraging steel.

According to the results obtained by other researchers, 3D printing can enhance the corrosion resistance of passive materials, while maraging steel is an active metal with a low corrosion rate. This study showed that SLM could not enhance the corrosion resistance of the active materials. It should be considered that SLM maraging steel has more grain boundaries and three times higher porosity fraction which all can deteriorate the corrosion resistance. In contrast, the corrosion resistance did not decrease.

The as-printed and heat-treated samples were immersed in 0.1 M NaCl, and pitting was observed on all samples after one day of immersion. Figure 11 demonstrates the SEM images and EDS maps of the corroded surfaces after rinsing with citric acid. Pits were observed on the surface of the samples. Figure 11(a) shows that pitting initiated at the melt pool boundaries on SLM sample where dendritic structure and the solute segregation happens. SEM and EDS maps (Fig. 11b–e) show the pit on AG, SLM sample, which exhibit that pitting started around Ti, Mo and V elements. The corrosion morphology (Fig. 11a) along with the EDS maps (Fig. 11c–e) confirms the segregation of Ti, Mo and V elements on the melt pool boundaries, which was not recognized by the EBSD phase map. Similar corrosion morphology was observed in conventional samples.

3.5 Electropolishing

As mentioned before, SLM sample has higher surface roughness than the conventional one. Bouzakis et al. (Ref 71), in their study, showed that maraging steel (18Ni-C300) round bar after turning and drilling had a surface roughness (R_a) around 1.2 µm, while the SLM sample had R_a value of around 11.8 µm. In this study, electropolishing was applied on SLM samples to investigate the surface roughness (R_a) reduction. For this purpose, polarization in electropolishing electrolyte was performed on *xy* plane of SLM samples to determine the proper potential for electropolishing. The relationship between current density (i) and electrochemical potential (anodic polarization) is shown in Fig. 12.

Anodic polarization curves have three distinct regions: the first stage showing a rapid increase in current with increase in

Table 3 The average values of nano-hardness and elastic modulus of *xy* plane of SLM and conventional samples at different conditions

	AP		AQ		AG
Conditions	**SLM**	**SLM**	**Conventional**	**SLM**	**Conventional**
Nano-hardness, GPa	4.1 ± 0.1	3.5 ± 0.1	3.7 ± 0.21	6.5 ± 0.6	6.3 ± 0.2
Elastic modulus, GPa	208 ± 11	220 ± 13	230 ± 22	233 ± 6	226 ± 14

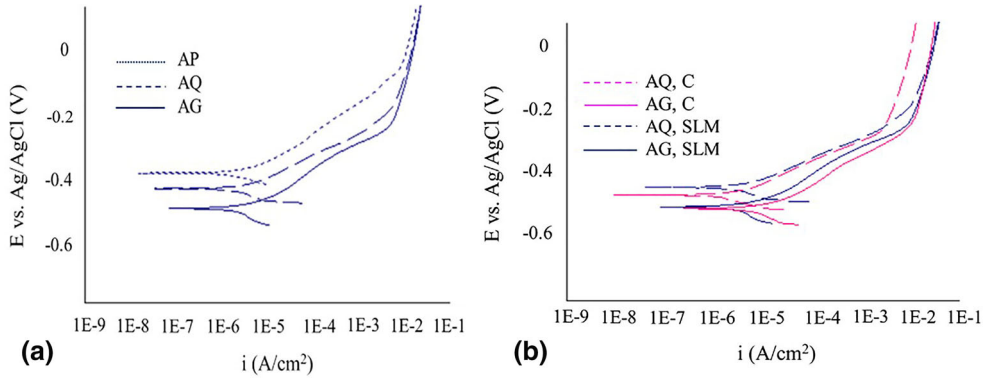

Fig. 10. Polarization curves in 0.5 M Na_2SO_4 for *xy* plane of (a) SLM sample, (b) conventional sample

Table 4 Corrosion current density and potential of SLM and conventional samples in 0.5 M Na_2SO_4 solution

Samples conditions	**AP, SLM**	**AQ, SLM**	**AG, SLM**	**C, AQ**	**C, AG**
i_{corr}, A cm^{-2}	2.7×10^{-6}	5.3×10^{-6}	4.2×10^{-6}	3.0×10^{-6}	4.4×10^{-6}
E_{corr}, V versus Ag/AgCl	− 0.36	− 0.40	− 0.46	− 0.43	− 0.47

potential, the second region, the plateau region, where current increases slowly with increase in potential, followed by the third region at higher potentials where there is a rapid increase in the current (Ref 72, 73).

Anodic dissolution begins during the first stage, and by increasing the voltage in the second stage, a steady state is reached where an oxide film forms on the maraging steel surface. Mass-transfer control is dominating in the second stage, where the rate of dissolution is limited due to the formation of the oxide film and indicates the optimal potential range for electropolishing (Ref 72, 74). Material removal is mainly even and constant during the plateau region (second region). By a further increase in potential, severe oxygen gas (O_2) evolution takes place and results in localized dissolution on the maraging steel surface.

SEM images in Fig. 13 demonstrate the effect of electropolishing potential on the surface morphologies of SLM samples. As-printed sample surface (Fig. 13a) possesses irregular features with isolated particles partially melted and adhered to the surface (R_a: 9.2 µm). At potentials lower than 3 V versus Ag/AgCl (Fig. 13b), polishing did not happen even though some rough areas were dissolved (R_a: 8.4 µm). In the potential range of 3-4 V versus Ag/AgCl (Fig. 13c), smoother surface was achieved, while due to unevenly distributed oxide film, the sample was not polished uniformly (R_a: 6.5 µm). The polished surface was obtained by polishing at 5 V versus Ag/AgCl (Fig. 13d, R_a: 3.2 µm), while higher potential, 6 V versus Ag/AgCl (Fig. 5e, R_a: 8.1 µm), leads to localized dissolution and, therefore, rougher surfaces.

According to the polarization curve (Fig. 12), conventional electropolishing for maraging steel should be run in the potential range of 0.05-2 V versus Ag/AgCl. While in this study, the polishing was negligible even by applying the maximum potential (2 V).

The surface roughness of the SLM parts consists of two types of surface profiles. One surface profile is due to the balling and staircases which depend on SLM process parameters (the reduced hatch spacing and powder layer thickness reduce the surface roughness) (Ref 20, 75, 76). The other surface profile is related to partially melted metal particles sticking on the as-printed side surface. The combination of these two surface profiles increases the difficulty in polishing SLM parts. Therefore, the conventional electropolishing process (which occurs in the second region of the polarization curve) might not be practical for SLM parts. As a result, overpotential electropolishing (by applying potential in the third region of polarization curve) is needed to face the high roughness and specific profile to remove the sticking particles. Macropolishing is based on the concept of Wagner number Eq 11 (Ref 77).

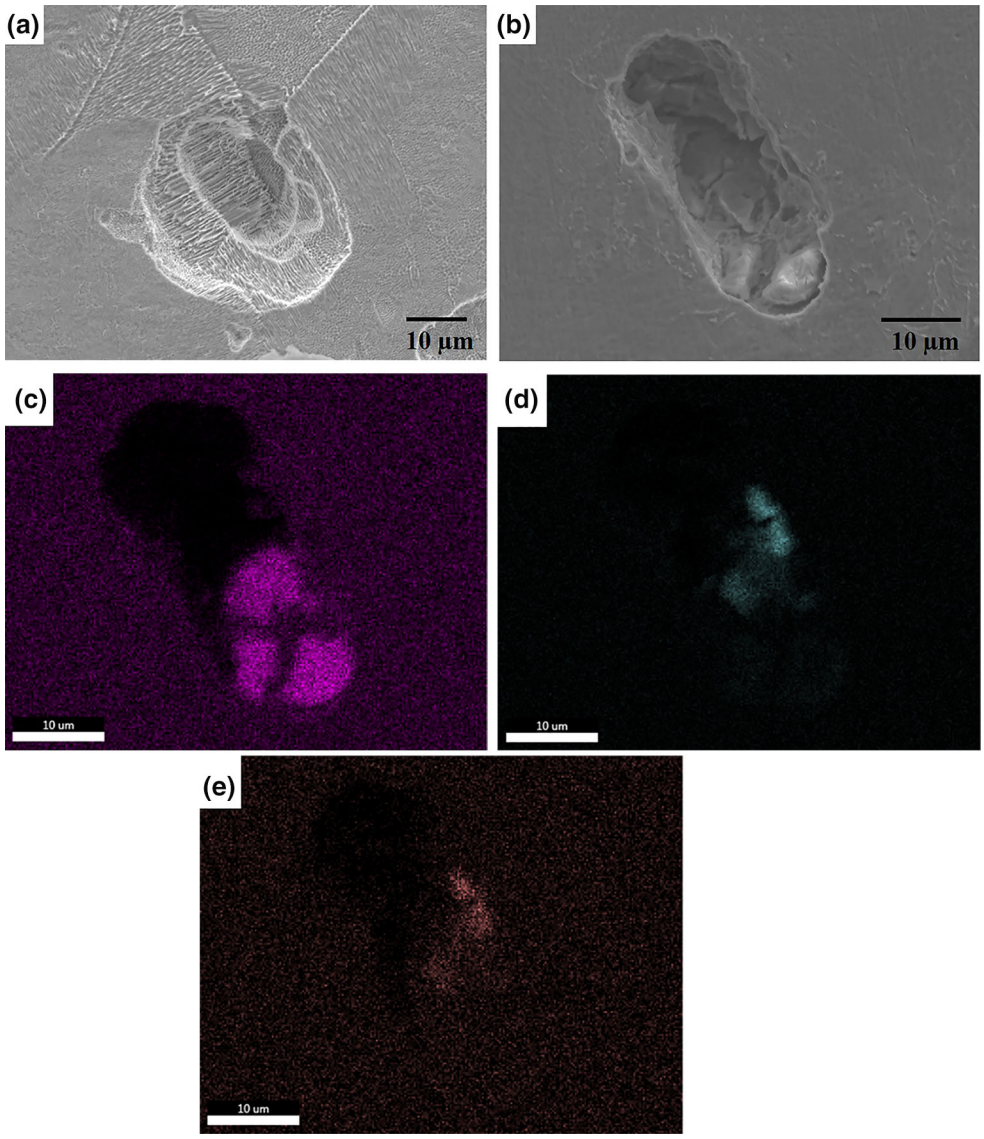

Fig. 11. SEM and EDS maps of the corroded *xy* plane after immersion for 1 day in 0.1 M NaCl, (a) AP, SLM, (b-e) AG, SLM, EDS map of (c) Mo, (d) Ti, (e) V

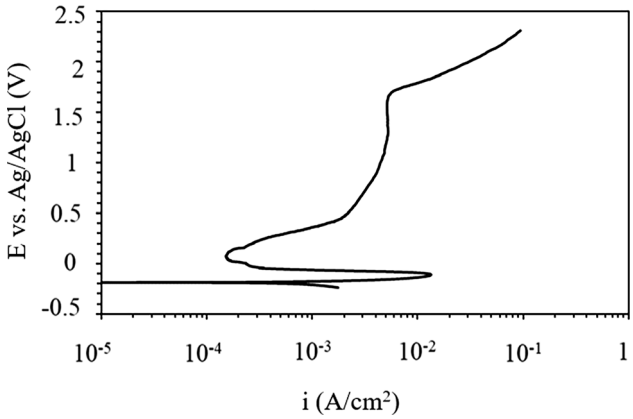

Fig. 12. Anodic polarization curve of SLM sample in electropolishing electrolyte at 60 °C

$$W_a = \frac{k\beta}{\mathrm{Li}_{\mathrm{ave}}} \quad \text{(Eq 11)}$$

where k is electrolyte conductivity, β is the Tafel coefficient, L is the characteristic length, and i_{ave} is the current density of the electropolishing process. Wagner number displays the ratio of faradic kinetic to electrolyte resistance. A higher Wagner number results in uniform current density distribution, which means the secondary current distribution (related to the dissolution) is dominated. At a lower Wagner number, the primary current distribution (controlled by the electrolyte resistance and therefore the surface geometry) dominates. Primary current distribution results in non-uniform current density on the sample surface, with higher dissolution rates on the peaks and lower in the valley, fostering a leveling effect.

According to Eq 11, a higher i_{ave} reduces the W_a, and therefore, the primary current distribution is dominant, which is favorable for electropolishing.

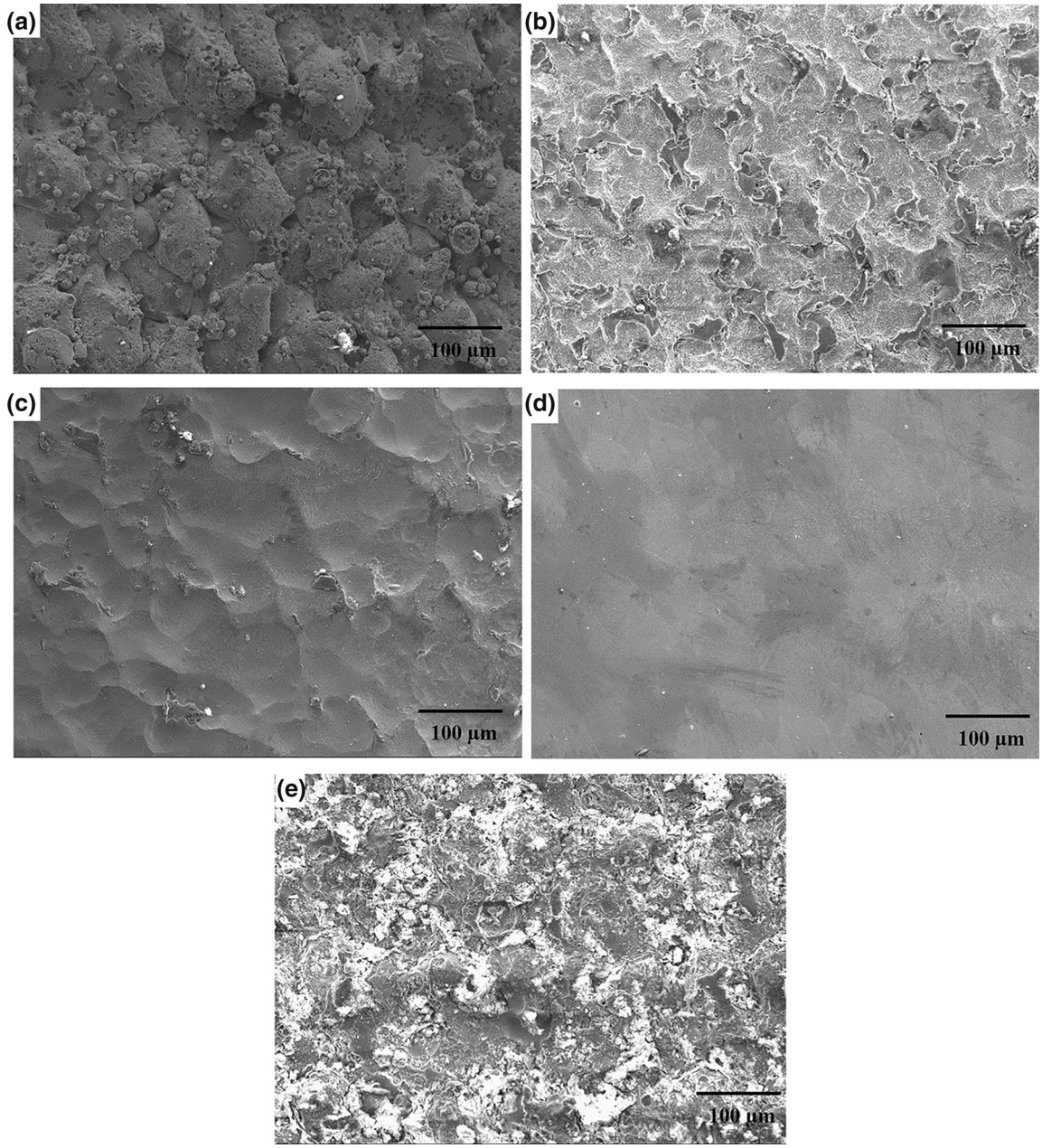

Fig. 13. SEM images of SLM samples (a) as-printed and after electropolishing for 20 min at (b) 3 V, (c) 4 V, (d) 5 V, (e) 6 V

Figure 14 displays the 2D profilometer images of the as-printed and electropolished (EP) samples. Confocal analysis was used on 0.7×0.7 cm^2 area to collect data from a large area. The results are listed in Table 5. Confocal analysis results disclosed that as-printed sample has S_a value of around 10.5 µm while by electropolishing at 5 V versus Ag/AgCl for 20 minutes, S_a value reduced to 3.7 µm.

There was a noticeable variation (S_z: 133 µm) in the height and depth of the surface features of the as-printed sample. According to Table 5, electropolishing for 20 min leads to the maximum polishing with a S_z value of 68 µm.

Results show a 23% thickness reduction after electropolishing. Even though surface roughness reduced by 65%, there is a challenge of geometry offset during part design and manufacturing.

4. Conclusions

In this study, maraging steel with a fine cellular structure was produced by the SLM process, and the following results were obtained.

1. The microstructure of the SLM sample possessed fine martensite without any strong texture, and there was no sign of anisotropy on different sections of the SLM sample.
2. Grain size in SLM samples after AQ and AG was about half of those in conventional wrought samples.
3. AQ increased the grain size of the SLM sample by 2.5 times, and by aging after AQ, the grain size was reduced but not as much as the one in AP condition.

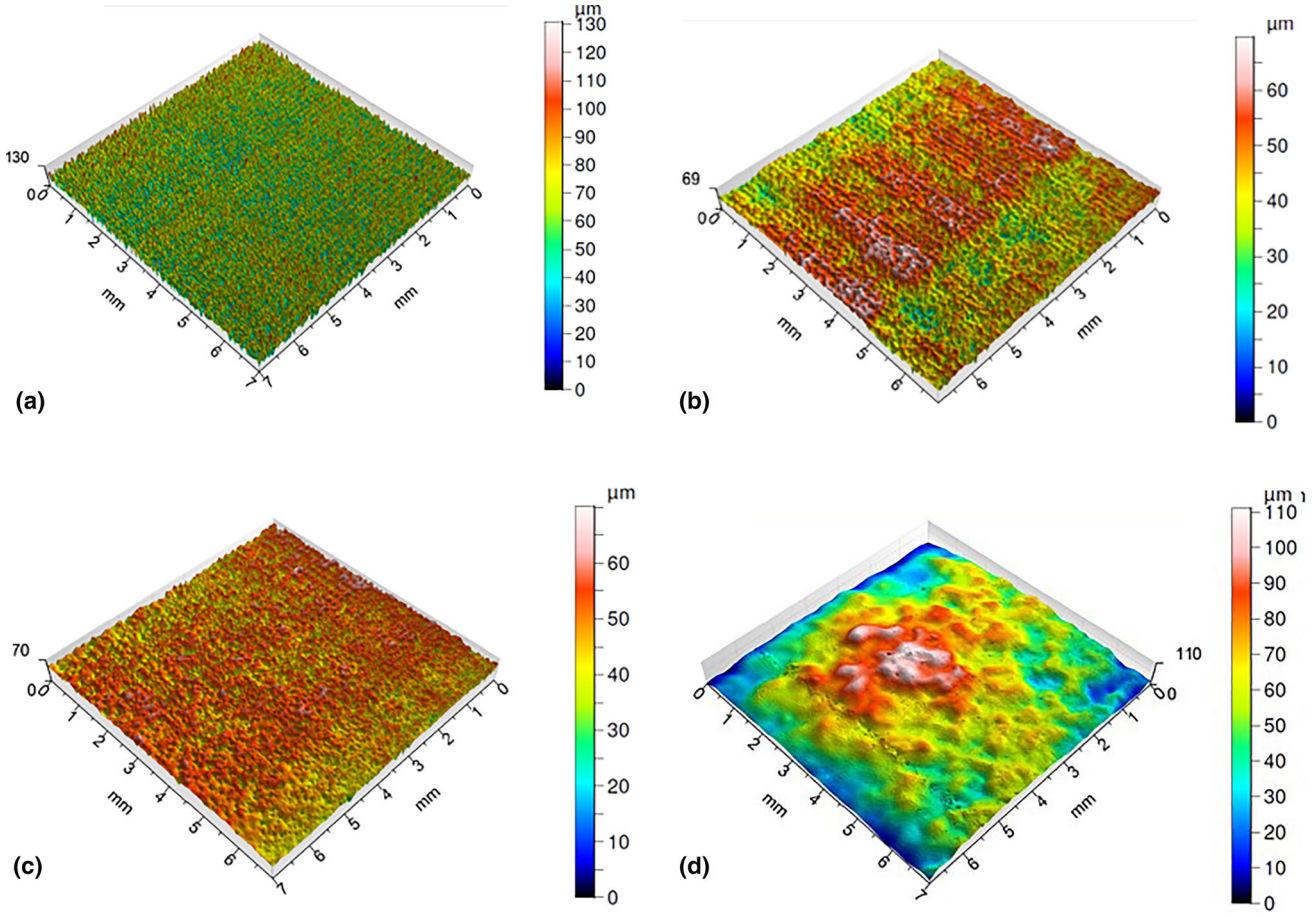

Fig. 14. Surface topography of (a) AP and EP samples at 5 V, (b) 10 min, (c) 20 min, (d) 30 min

Table 5 Surface profiles parameters of AP and EP samples

Conditions	S_a, µm	S_q, µm	S_p, µm	S_v, µm	S_z, µm
AP	10.5 ± 0.5	13.0 ± 0.5	70.1 ± 5.0	63.4 ± 0.9	133.5 ± 6.4
EP, 5 V, 10 min	8.0 ± 0.5	10.7 ± 1.2	50.6 ± 0.6	74.3 ± 1.5	125.0 ± 1.2
EP, 5 V, 20 min	3.7 ± 0.3	4.8 ± 0.5	21.0 ± 1.5	47.1 ± 1.2	68.2 ± 2.4
EP, 5 V, 30 min	9.8 ± 1.1	12.7 ± 1.9	63.6 ± 10.5	52.9 ± 13.2	116.7 ± 25.1

4. Despite the finer microstructure of SLM maraging steel, similar nano-hardness values as conventional ones were obtained, which revealed that precipitation is the main strengthening mechanism in maraging steel.
5. Aging resulted in the maximum nano-hardness of maraging steel (1.6 times that of in AP SLM), while it reduced its corrosion resistance slightly. The corrosion rate was increased around 1.5 times, and corrosion potential was decreased 100 mV.
6. Higher porosity percentages and grain boundaries, along with smaller intermetallic size, result in comparable corrosion properties of conventional and SLM samples.
7. Melt pool boundaries, enriched with retained austenite and intermetallics, were the susceptible places for corrosion in the SLM sample.
8. Surface roughness analysis proved that the electropolishing process improved the overall roughness, smoothened the profiles, and homogenized the peaks and valleys.
9. The smoothest surface was obtained by electropolishing at 5 V versus Ag/AgCl for 20 min, which reduced the R_a value of the AP sample by 65%.

Acknowledgments

The financial support by Åforsk under Agreement No. 18466 is acknowledged.

Funding

Open access funding provided by Jönköping University.

References

1. T.D. Ngo, A. Kashani, G. Imbalzano, K.T.Q. Nguyen, and D. Hui, Additive Manufacturing (3D Printing): A Review of Materials, Methods, Applications and Challenges, *Compos. Part B Eng.*, 2018, **143**(43), p 172–196. https://doi.org/10.1016/j.compositesb.2018.02.012
2. I. Bahnini, M. Rivette, A. Rechia, A. Siadat, and A. Elmesbahi, Additive Manufacturing Technology: The Status, Applications, and Prospects, *Int. J. Adv. Manufac. Technol.*, 2018, **97**, p 147–161
3. T.H. Becker and D. Dimitrov, The Achievable Mechanical Properties of SLM Produced Maraging Steel 300 Components, *R. Prototype*, 2016, **22**, p 487–494. https://doi.org/10.1108/RPJ-08-2014-0096
4. D. Herzog, V. Seyda, E. Wycisk, and C. Emmelmann, Additive Manufacturing of Metals, *Acta Mater.*, 2016, **117**, p 371–392. https://doi.org/10.1016/j.actamat.2016.07.019
5. A. Leon, A. Shirizly, and E. Aghion, Corrosion Behavior of AlSi10Mg Alloy Produced by Additive Manufacturing (AM) vs. Its Counterpart Gravity Cast Alloy, *Metals*, 2016, **6**, p 148–157. https://doi.org/10.3390/met6070148
6. J. Suryawanshi, T. Baskaran, O. Prakash, S.B. Arya, and U. Ramamurty, On the Corrosion Resistance of Some Selective Laser Melted Alloys, *Materialia*, 2018, **3**, p 153–161. https://doi.org/10.1016/j.mtla.2018.08.022
7. C. Tan, K. Zhou, M. Kuang, W. Ma, T. Kuang, and C. Tan, Microstructural Characterization and Properties of Selective Laser Melted Maraging Steel with Different Build Directions Maraging Steel with Different Build Directions, *Sci. Technol. Adv. Mater.*, 2018, **19**, p 746–758. https://doi.org/10.1080/14686996.2018.1527645
8. Y. Bai, Y. Yang, D. Wang, and M. Zhang, Influence Mechanism of Parameters Process and Mechanical Properties Evolution Mechanism of Maraging Steel 300 by Selective Laser Melting, *Mater. Sci. Eng. A.*, 2017, **703**, p 116–123. https://doi.org/10.1016/j.msea.2017.06.033
9. X. Cui, S. Zhang, C. Wang, C.H. Zhang, J. Chen, and J.B. Zhang, Microstructure and Fatigue Behavior of a Laser Additive Manufactured 12CrNi2 Low Alloy Steel, *Mater. Sci. Eng. A.*, 2020, **772**, p 138685. https://doi.org/10.1016/j.msea.2019.138685
10. X. Ran, D. Liu, J. Li, H. Wang, X. Cheng, and J. Zhang, Effects of Microstructures on the Fatigue Crack Growth Behavior of Laser Additive Manufactured Ultrahigh-Strength AerMet100 Steel, *Mater. Sci. Eng. A*, 2018, **721**, p 251–262. https://doi.org/10.1016/j.msea.2018.02.088
11. J.P. Oliveira, A.D. Lalonde, and J. Ma, Processing Parameters in Laser Powder Bed Fusion Metal Additive Manufacturing, *Mater. Des.*, 2020, **193**, p 1–12. https://doi.org/10.1016/j.matdes.2020.108762
12. F.F. Conde, J.D. Escobar, J.P. Oliveira, A.L. Jardini, W.W.B. Filho, and J.A. Avila, Austenite Reversion Kinetics and Stability During Tempering of an Additively Manufactured Maraging 300 Steel, *Addit. Manuf.*, 2019, **29**, p 100804. https://doi.org/10.1016/j.addma.2019.100804
13. J.R. Scully and N. Birbilis, Corrosion of Additively Manufactured Alloys: A Review, *Corrosion*, 2018, **74**, p 1318–1350
14. B. Mooney, K.I. Kourousis, and R. Raghavendra, Plastic Anisotropy of Additively Manufactured Maraging Steel: Influence of the Build Orientation and Heat Treatments, *Addit. Manuf.*, 2019, **25**, p 19–31. https://doi.org/10.1016/j.addma.2018.10.032
15. E. Wycisk, A. Solbach, S. Siddique, D. Herzog, and F. Walther, Effects of Defects in Laser Additive Manufactured Ti-6Al-4V on Fatigue Properties, *Phys. Proc.*, 2014, **56**, p 371–378. https://doi.org/10.1016/j.phpro.2014.08.120
16. K. Kempen, E. Yasa, L. Thijs, J. Kruth, and J. Van Humbeeck, Microstructure and Mechanical Properties of Selective Laser Melted, *Phys. Proc.*, 2011, **12**, p 255–263. https://doi.org/10.1016/j.phpro.2011.03.033
17. G. Casalino, S.L. Campanelli, N. Contuzzi, and A.D. Ludovico, Experimental Investigation and Statistical Optimisation of the Selective Laser Melting Process of a Maraging Steel, *Opt. Laser Technol.*, 2015, **65**, p 151–158. https://doi.org/10.1016/j.optlastec.2014.07.021
18. J. Suryawanshi, K.G. Prashanth, and U. Ramamurty, Tensile, Fracture, and Fatigue Crack Growth Properties of a 3D Printed Maraging Steel Through Selective Laser Melting, *J. Alloys Compd.*, 2017, **725**, p 355–364. https://doi.org/10.1016/j.jallcom.2017.07.177
19. G. Strano, L. Hao, R.M. Everson, and K.E. Evans, Surface Roughness Analysis, Modelling and Prediction in Selective Laser Melting, *J. Mater. Process. Technol.*, 2013, **213**, p 589–597. https://doi.org/10.1016/j.jmatprotec.2012.11.011
20. R. Li, J. Liu, Y. Shi, and L. Wang, Balling Behavior of Stainless steel and Nickel Powder During Selective Laser Melting Process, *Int. J. Adv. Manuf. Technol.*, 2012, **59**, p 1025–1035. https://doi.org/10.1007/s00170-011-3566-1
21. K. Alrbaey, D. Wimpenny, R. Tosi, W. Manning, and A. Moroz, On Optimization of Surface Roughness of Selective Laser Melted Stainless Steel Parts: A Statistical Study, *J. Mater. Eng. Perform.*, 2014, **23**, p 2139–2148. https://doi.org/10.1007/s11665-014-0993-9
22. T.S.N.S. Narayanan, J. Kim, H. Eui, and H. Wook, Enhancement of the Surface Properties of Selective Laser Melted Maraging Steel by Large Pulsed Electron-Beam Irradiation, *Addit. Manuf.*, 2020, **33**, p 101125. https://doi.org/10.1016/j.addma.2020.101125
23. J.G. Lopes, C.M. Machado, V.R. Duarte, T.A. Rodrigues, T.G. Santos, and P. Oliveira, Effect of Milling Parameters on HSLA Steel Parts Produced by Wire and Arc Additive Manufacturing (WAAM), *J. Manuf. Process.*, 2020, **59**, p 739–749
24. B. Vayssette, N. Saintier, C. Brugger, B. Vayssette, and B. Vayssette, Surface Roughness of Ti-6Al-4V Parts Obtained by SLM and EBM. Effect on the High Cycle Fatigue, *Proc. Eng.*, 2018, **213**, p 89–97. https://doi.org/10.1016/j.proeng.2018.02.010
25. Y. Kaynak and O. Kitay, Porosity, Surface Quality, Microhardness and Microstructure of Selective Laser Melted 316L Stainless Steel Resulting from Finish Machining, *J. Manuf. Mater. Process.*, 2018 https://doi.org/10.3390/jmmp2020036
26. D. Shamvedi, C. Danilenkoff, P.O. Leary, and R. Raghavendra, Investigation of the Influence of Build Orientation on the Surface Roughness of the 3D Metal Printed Horn Antenna, in *12th European Conference on Antennas and Propagation*. April 2018, UK. https://doi.org/10.1049/cp.2018.0680
27. T. Goulet, C. Riso, R. Stephenson, N. Chuenprateep, R. Knott, A. Reddick, J. Schlitzer, C. Benton, and F. Garcia-moreno, Reducing the Roughness of Internal Surface of an Additive Manufacturing Produced Steel Component by Chempolishing and Electropolishing, *Addit. Manuf.*, 2019, **25**, p 32–38
28. T. Bhardwaj and M. Shukla, Direct Metal Laser Sintering of Maraging Steel: Effect of Building Orientation on Surface Roughness and Microhardness, *Mater. Today Proc.*, 2018, **5**, p 20485–20491. https://doi.org/10.1016/j.matpr.2018.06.425
29. S. Sneddon, Y. Xu, M. Dixon, D. Rugg, P. Li, and D.M. Mulvihill, Sensitivity of Material Failure to Surface Roughness: A Study on Titanium Alloys Ti64 and Ti407, *Mater. Des.*, 2021, **200**, p 109438. https://doi.org/10.1016/j.matdes.2020.109438
30. S. Mok, W. Gyu, Y. Ho, and H. Jang, Surface Roughness and the Corrosion Resistance of 21Cr Ferritic Stainless Steel, *Corros. Sci.*, 2012, **63**, p 404–409. https://doi.org/10.1016/j.corsci.2012.06.031

31. A. Fortunato, A. Lulaj, S. Melkote, E. Liverani, A. Ascari, and D. Umbrello, Milling of Maraging Steel Components Produced by Selective Laser Melting, *Int. J. Adv. Manuf. Technol.*, 2018, **94**, p 1895–1902. https://doi.org/10.1007/s00170-017-0922-9
32. W.J. Wang, K.C. Yung, H.S. Choy, T.Y. Xiao, and Z.X. Cai, Effects of Laser Polishing on Surface Microstructure and Corrosion Resistance of Additive Manufactured CoCr Alloys, *Appl. Surf. Sci.*, 2018, **443**, p 167–175
33. P. Tyagi, T. Goulet, C. Riso, and F. Garcia-Moreno, Reducing Surface Roughness by Chemical Polishing of Additively Manufactured 3D Printed 316 Stainless Steel Components, *Int. J. Adv. Manuf. Technol.*, 2019, **100**, p 2895–2900
34. G. Yang, B. Wang, K. Tawfiq, H. Wei, S. Zhou, and G. Chen, Electropolishing of Surfaces: Theory and Applications, *Surf. Eng.*, 2016, **112**, p 149–166. https://doi.org/10.1080/02670844.2016.1198452
35. U. Su, K. Jeong, and W. Park, High-Quality Surface Finishing of Industrial Three-Dimensional Metal Additive Manufacturing Using Electrochemical Polishing, *Int. J. Precis. Eng. Manuf. Technol.*, 2019, **6**, p 11–21. https://doi.org/10.1007/s40684-019-00019-2
36. B.G. Pyka, A. Burakowski, G. Kerckhofs, M. Moesen, S. Van Bael, J. Schrooten, and M. Wevers, Surface Modification of Ti6Al4V Open Porous Structures Produced by Additive Manufacturing, *Addit. Manuf.*, 2012, **5**, p 363–370. https://doi.org/10.1002/adem.201100344
37. C. Carson, *Heat Treating of Maraging Steels*, Vol 4 ASM Handbook, Materials Park, 2014, p 468–480. https://doi.org/10.31399/asm.hb.v04d.a0005948
38. C.R. Shamantha, R. Narayanan, K.J.L. Iyer, and V.M. Radhakrishnan, Microstructural Changes During Welding and Subsequent Heat Treatment of 18Ni (250-grade) Maraging Steel, *Mater. Sci. Eng. A.*, 2000, **287**, p 43–51
39. G. Krauss and A.R. Marder, The Morphology of Martensite in Iron Alloys, *Metall. Trans.*, 1971, **2**, p 2343–2357
40. Y. Bai, D. Wang, Y. Yang, and H. Wang, Effect of Heat Treatment on the Microstructure and Mechanical Properties of Maraging Steel by Selective Laser Melting, *Mater. Sci. Eng. A.*, 2019, **760**, p 105–117. https://doi.org/10.1016/j.msea.2019.05.115
41. X. Liu, C. Zhao, X. Zhou, Z. Shen, and W. Liu, Microstructure of Selective Laser Melted AlSi10Mg Alloy, *Mater. Des.*, 2019, **168**, p 1–9. https://doi.org/10.1016/j.matdes.2019.107677
42. R. Casati, J. Lemke, and M. Vedani, Microstructure and Fracture Behavior of 316L Austenitic Stainless Steel Produced by Selective Laser Melting, *J. Mater. Sci. Technol.*, 2016, **32**, p 738–744. https://doi.org/10.1016/j.jmst.2016.06.016
43. C. Tan, K. Zhou, W. Ma, P. Zhang, M. Liu, and T. Kuang, Microstructural Evolution, Nanoprecipitation Behavior and Mechanical Properties of Selective Laser Melted High-Performance Grade 300 Maraging Steel, *Mater. Des.*, 2017, **134**, p 23–34. https://doi.org/10.1016/j.matdes.2017.08.026
44. L. Thijs, F. Verhaeghe, T. Craeghs, J. Van Humbeeck, and J. Kruth, A Study of the Microstructural Evolution During Selective Laser Melting of Ti-6Al-4V, *Acta Mater.*, 2010, **58**, p 3303–3312. https://doi.org/10.1016/j.actamat.2010.02.004
45. H. Chen, D. Gu, D. Dai, M. Xia, and C. Ma, A Novel Approach to Direct Preparation of Complete Lath Martensite Microstructure in Tool Steel by Selective Laser Melting, *Mater. Lett.*, 2018, **227**, p 128–131. https://doi.org/10.1016/j.matlet.2018.05.042
46. E.A. Jägle, Z. Sheng, P. Kürnsteiner, S. Ocylok, A. Weisheit, and D. Raabe, Comparison of Maraging Steel Micro- and Nanostructure Produced Conventionally and by Laser Additive Manufacturing, *Materials*, 2017, **10**, p 8–23. https://doi.org/10.3390/ma10010008
47. M.G. Collins, A.J. Ramirez, and J.C. Lippold, An Investigation of Ductility Dip Cracking in Nickel-Based Weld Metals—Part II, *Weld. J.*, 2003, **39**, p 348–354
48. A.J. Ramirez, J.W. Sowards, and J.C. Lippold, Improving the Ductility-Dip Cracking Resistance of Ni-Base Alloys, *J. Mater. Proc. Technol.*, 2006, **179**, p 212–218. https://doi.org/10.1016/j.jmatprotec.2006.03.095
49. X.Y. Fang, H.Q. Li, M. Wang, C. Li, and Y.B. Guo, Characterization of Texture and Grain Boundary Character Distributions of Selective Laser Melted Inconel 625 Alloy, *Mater. Charact.*, 2018, **143**, p 182–190. https://doi.org/10.1016/j.matchar.2018.02.008
50. H. Kitahara, R. Ueji, N. Tsuji, and Y. Minamino, Crystallographic Features of Lath Martensite in Low-Carbon Steel, *Acta Mater.*, 2006, **54**, p 1279–1288. https://doi.org/10.1016/j.actamat.2005.11.001
51. R. Ueji, N. Tsuji, Y. Minamino, and Y. Koizumi, Ultragrain Refinement of Plain Low Carbon Steel by Cold-Rolling and Annealing of Martensite, *Acta Mater.*, 2002, **50**, p 4177–4189
52. J. Mutua, S. Nakata, T. Onda, and Z. Chen, Optimization of Selective Laser Melting Parameters and Influence of Post Heat Treatment on Microstructure and Mechanical Properties of Maraging Steel, *Mater. Des.*, 2018, **139**, p 486–497. https://doi.org/10.1016/j.matdes.2017.11.042
53. S. Li, Q. Wei, Y. Shi, Z. Zhu, and D. Zhang, Microstructure Characteristics of Inconel 625 Superalloy Manufactured by Selective Laser Melting, *J. Mater. Sci. Technol.*, 2015, **31**, p 946–952. https://doi.org/10.1016/j.jmst.2014.09.020
54. A. Kreitcberg, V. Brailovski, and S. Turenne, Effect of Heat Treatment and Hot Isostatic Pressing on the Microstructure and Mechanical Properties of Inconel 625 Alloy Processed by Laser Powder Bed Fusion, *Mater. Sci. Eng. A.*, 2017, **689**, p 1–10. https://doi.org/10.1016/j.msea.2017.02.038
55. W.D. Callister and D. Rethwisch, *Materials Science and Engineering*, 8th ed. Wiley, New York, 2006, p 577–620
56. P. Gao, G. Jing, X. Lan, S. Li, Y. Zhou, Y. Wang, H. Yang, K. Wei, and Z. Wang, Effect of Heat Treatment on Microstructure and Mechanical Properties of Fe–Cr–Ni–Co–Mo Maraging Stainless Steel Produced by Selective Laser Melting, *Mater. Sci. Eng. A*, 2021, **814**, p 141149. https://doi.org/10.1016/j.msea.2021.141149
57. S. Sarkar, S. Mukherjee, C. Siva, and A. Kumar, Effects of Heat Treatment on Microstructure, Mechanical and Corrosion Properties of 15–5 PH Stainless Steel Parts Built by Selective Laser Melting Process, *J. Manuf. Process.*, 2020, **50**, p 279–294. https://doi.org/10.1016/j.jmapro.2019.12.048
58. Y. Li, W. Yan, J.D. Cotton, G.J. Ryan, Y. Shen, W. Wang, and Y. Shan, A New 1.9 GPa Maraging Stainless Steel Strengthened by Multiple Precipitating Species, *Mater. Des.*, 2015, **82**, p 56–63. https://doi.org/10.1016/j.matdes.2015.05.042
59. J. Song, Q. Tang, Q. Feng, S. Ma, R. Setchi, Y. Liu, and Q. Han, Effect of Heat Treatment on Microstructure and Mechanical Behaviours of 18Ni-300 Maraging Steel Manufactured by Selective Laser Melting, *Opt. Laser Technol.*, 2019, **120**, p 105725. https://doi.org/10.1016/j.optlastec.2019.105725
60. F.F. Conde, J.D. Escobar, J.P. Oliveira, M. Béreš, A.L. Jardini, W. Bose, and J.A. Avila, Effect of Thermal Cycling and Aging Stages on the Microstructure and Bending Strength of a Selective Laser Melted 300-Grade Maraging Steel, *Mater. Sci. Eng. A.*, 2019, **758**, p 192–201. https://doi.org/10.1016/j.msea.2019.03.129
61. W.C. Oliver and G.M. Pharr, An Improved Technique for Determining Hardness and Elastic Modulus Using Load and Displacement Sensing Indentation Experiments, *J. Mater. Res.*, 1992, **7**, p 1564–1583
62. W.C. Oliver and G.M. Pharr, Measurement of Hardness and Elastic Modulus by Instrumented Indentation: Advances in Understanding and Refinements to Methodology, *J. Mater. Res.*, 2004, **19**, p 3–20. https://doi.org/10.1557/jmr.2004.19.1.3
63. R. Saha and W.D. Nix, Effects of the Substrate on the Determination of thin Film Mechanical Properties by Nanoindentation, *Acta Mater.*, 2002, **50**, p 23–38
64. Y.W. Bao, W. Wang, and Y.C. Zhou, Investigation of the Relationship Between Elastic Modulus and Hardness Based on Depth-Sensing Indentation Measurements, *Acta Mater.*, 2004, **52**, p 5397–5404. https://doi.org/10.1016/j.actamat.2004.08.002
65. A.F. Avelino, W.S. Araújo, D.F. Dias, L. Paulo, M. Santos, A.N. Correia, and P. De Lima-neto, Corrosion Investigation of the 18Ni 300 Grade Maraging Steel in Aqueous Chloride Medium Containing H_2S and CO_2, *Electrochim. Acta.*, 2018, **286**, p 339–349. https://doi.org/10.1016/j.electacta.2018.08.042
66. K.M. Mantrala and V.K. Balla, Additive Manufacturing of Co-Cr-Mo Alloy: Influence of Heat Treatment on Microstructure, Tribological, and Electrochemical Properties, *Front. Mech. Eng.*, 2015, **1**, p 1–7. https://doi.org/10.3389/fmech.2015.00002
67. A.G. Demir and B. Previtali, Investigation of Remelting and Preheating in SLM of 18Ni300 Maraging Steel as Corrective and Preventive Measures for Porosity Reduction, *Int. J. Adv. Manuf. Technol.*, 2017, **93**, p 2697–2709. https://doi.org/10.1007/s00170-017-0697

68. Y. Sun, A. Moroz, and K. Alrbaey, Sliding Wear Characteristics and Corrosion Behaviour of Selective Laser Melted 316L Stainless Steel, *J. Mater. Eng. Perform.*, 2014, **23**, p 518–526. https://doi.org/10.1007/s11665-013-0784-8
69. D. Kong, C. Dong, X. Ni, L. Zhang, J. Yao, C. Man, X. Cheng, K. Xiao, and X. Li, Mechanical Properties and Corrosion Behavior of Selective Laser Melted 316L Stainless Steel After Different Heat Treatment Processes, *J. Mater. Sci. Technol.*, 2019, **35**, p 1499–1507. https://doi.org/10.1016/j.jmst.2019.03.003
70. X. Ni, D. Kong, W. Wu, L. Zhang, C. Dong, B. He, L. Lu, K. Wu, and D. Zhu, Corrosion Behavior of 316L Stainless Steel Fabricated by Selective Laser Melting Under Different Scanning Speeds, *J. Mater. Eng. Perform.*, 2018, **27**, p 3667–3677. https://doi.org/10.1007/s11665-018-3446-z
71. N. Michailidis, P. Stief, J. Dantan, A. Etienne, and A. Siadat, Comparison of Additively Manufactured vs. Conventional Maraging Steel in Corrosion-Fatigue Performance After Variouse Surface Treatments, *Proc. CIRP*, 2020, **87**, p 469–473. https://doi.org/10.1016/j.procir.2020.03.003
72. M. Ziomek-Moroz, *Electropolishing, Corrosion: Fundamentals, Testing, and Protection*, Vol 13 ASM Handbook, Materials Park, 2003, p 139–142. https://doi.org/10.31399/asm.hb.v13a.a0003595
73. P. Neufeld and T. Zervas, The Relationship Between Polarisation Characteristics an the Electropolishing Behaviour of Copper, *Surf. Technol.*, 1979, **8**, p 129–135
74. G. Yang, O. Ridge, H. Wei, and G. Chen, Electropolishing of Surfaces: Theory and Applications, *Surf. Eng.*, 2016, **33**, p 149–166. https://doi.org/10.1080/02670844.2016.1198452
75. F. Cabanettes, A. Joubert, G. Chardon, V. Dumas, J. Rech, C. Grosjean, and Z. Dimkovski, Topography of as Built Surfaces Generated in Metal Additive Manufacturing: A Multi Scale Analysis from Form to Roughness, *Percis. Eng.*, 2018, **52**, p 249–265. https://doi.org/10.1016/j.precisioneng.2018.01.002
76. S. Liu and H. Guo, Balling Behavior of Selective Laser Melting (SLM) Magnesium Alloy, *Materials*, 2020, **13**(16), p 3632
77. J. Han, J. Han, B. Soo Lee, J. Lim, S. Kim, H. Kim, and S. Kang, Elimination of Nanovoids Induced During Electroforming of Metallic Nanostamps with High Aspect Ratio Nanostructures by the Pulse Reverse Current Electroforming Process, *J. Micromech. Micoeng.*, 2012, **22**, p 65004